coatings

MDPI

Article

Rational Design of Hollow Glass Microspheres/Urushiol Titanium Polymer–Zirconium Phosphate Coating System with Synergistic Anticorrosion Function for Waterborne Epoxy Resin

Xiaoxiao Zheng, Runhui Mao, Mingmin Li, Jipeng Chen, Fengcai Lin, Donghui Wang, Guocai Zheng, Yanlian Xu * and Qi Lin *

Fuzhou Institute of Oceanography, Fujian Engineering and Research Center of New Chinese Lacquer Materials, College of Materials and Chemical Engineering, Minjiang University, Fuzhou 350108, China; xxzheng@mju.edu.cn (X.Z.); m19859325876@163.com (R.M.); 17850873748@163.com (M.L.); jpchen@mju.edu.cn (J.C.); linfengcai8@163.com (F.L.); dwang@mju.edu.cn (D.W.); guocaizheng@mju.edu.cn (G.Z.)
* Correspondence: ylxu@mju.edu.cn (Y.X.); qlin1990@163.com (Q.L.)

Abstract

To tackle the long-standing issue of inadequate corrosion protection in waterborne coatings, this study innovatively incorporates hollow glass microspheres (HGB) into waterborne epoxy zinc-rich primers through physical blending, constructing a dual-layer synergistic anticorrosion system comprising an HGB-modified primer and a zirconium phosphate/urushiol titanium polymer (UTPCZrP)-modified waterborne epoxy topcoat. Optimal performance is achieved with 2 wt% HGB addition: the dual-layer coating retains favorable physicochemical and mechanical properties while enhancing anticorrosion performance by 1–2 orders of magnitude, boasting an impedance of 3.2×10^6 Ω, a corrosion rate as low as 5.71×10^{-6} mm/year, 99.98% protection efficiency (stable after 25-day immersion), and 720 h salt spray resistance without corrosion diffusion. This method exhibits universality in waterborne polyurethane (WPU) and polyester (WPE) systems, yielding impedance values of 3.57×10^6 Ω and 2.7×10^6 Ω, respectively, with over 90% improved anticorrosion performance and long-term stability. By optimizing components and synergistic system design, this work significantly enhances waterborne coatings' anticorrosion efficiency, reduces raw material costs, and provides a scalable technical pathway for high-performance, eco-friendly anticorrosion coatings.

Keywords: anticorrosive coatings; waterborne epoxy resin; hollow glass microspheres; urushiol titanium polymer

Check for updates

Academic Editor: Maria Vittoria Diamanti

Received: 31 December 2025
Revised: 7 February 2026
Accepted: 11 February 2026
Published: 13 February 2026

Copyright: © 2026 by the authors. Licensee MDPI, Basel, Switzerland. This article is an open access article distributed under the terms and conditions of the Creative Commons Attribution (CC BY) license.

1. Introduction

Metal materials face dual challenges of electrochemical and chemical corrosion in industrial applications, causing economic losses of hundreds of billions of dollars annually and posing serious threats to safety production and ecological balance [1,2]. Although traditional organic coatings exhibit excellent performance, their environmental impact stemming from the release of volatile organic compounds (VOCs) released during their production and use limit their sustainable development [3]. Waterborne coatings, using water as the dispersion medium, offer core environmental advantages such as zero VOCs and low toxicity, making them an important research direction in the field of green anticorrosion [4]. However, the development and application scale of waterborne anticorrosive coatings in China still lag behind Europe, where large-scale industrialization has been

achieved. Therefore, developing high-performance waterborne anticorrosive coatings with independent intellectual property rights is crucial for China's industrial upgrading.

Waterborne epoxy resin (WEP) represents a prominent environmentally friendly matrix widely employed in protective coatings [5], finding applications across diverse sectors such as construction materials, chemical processing, and aerospace due to its exceptional adhesive strength, mechanical robustness, and resistance to chemical degradation [6,7]. Furthermore, its ease of modification offers significant versatility for tailored performance. Nevertheless, WEP suffers from several critical drawbacks, including high raw material costs, a relatively slow curing process and coating water resistance that requires further improvement; and inherent molecular chain characteristics that impose restrictions on UV aging resistance, mechanical integrity, thermal stability, and long-term anticorrosion performance [8]. These limitations necessitate urgent research and development efforts to enhance its practical utility and service life in demanding environments [9].

Within anticorrosive coating systems, epoxy zinc-rich primers function as a critical first-line protection, with their core mechanism relying on the cathodic protection effect formed by the contact between zinc powder particles and the metal substrate [10–12]. Although the electrical continuity diminishes as zinc is consumed electrochemically, the resulting zinc corrosion products contribute to a secondary barrier effect by suppressing anodic activity and sealing micro-pores within the coating matrix. However, the high cost of zinc powder severely compresses product profit margins, necessitating technological innovation to achieve cost reduction and efficiency improvement.

Hollow glass microspheres (HGB), are a type of micron-sized hollow spherical inorganic fillers, characterized by low density, low dielectric constant, high compressive strength, excellent thermal stability, and chemical inertness [13,14]. Owing to their unique hollow spherical architecture, HGB not only suppress the sedimentation of zinc powder in zinc-rich primers, enhance the rheological properties of the system, reduce internal coating stress, and hinder crack propagation, but also act synergistically with flake-shaped fillers to create a "labyrinth effect" that significantly prolonging the penetration path of corrosive media, thereby enhancing the overall physical barrier and long-term protection capabilities of the coating [15,16]. Although the incorporation of non-conductive HGB may partially reduce the electrical connectivity among zinc particles, the zinc content remains sufficiently high to maintain effective cathodic protection. The primary role of zinc is to provide initial sacrificial anode protection at defects and to subsequently form corrosion products that seal micro-pores, while HGB enhances the physical barrier through defect filling and the labyrinth effect. This design strategically leverages the synergy between zinc's electrochemical activity and HGB's barrier enhancement, rather than aiming for a complete replacement of zinc's function.

To address the contradiction between the anticorrosion performance and cost-effectiveness of waterborne coatings, this study constructs a dual-layer synergistic anticorrosion system based on a rational design strategy. The design criteria focused on enhancing corrosion protection while reducing costs. HGB was selected for the primer due to its cost-effectiveness and unique functional properties, including creating a synergistic "labyrinth effect". AUZ was chosen for the topcoat owing to the superior barrier properties of UTP and ZrP, with a concentration of 5 wt% determined as optimal to maximize performance while maintaining coating integrity. The dual-layer architecture was designed to leverage the cathodic protection of the zinc-rich primer and the enhanced physical/chemical barrier of the AUZ topcoat synergistically: the bottom layer prepares HGB-modified waterborne epoxy zinc-rich primers by partially replacing high-cost zinc powder with HGB; the top layer is matched with a high-performance waterborne coating modified with 5 wt% AUZ to enhance barrier and corrosion inhibition functions, and

the film-forming substance of the topcoat is extended from WEP to WPU and WPE to verify the system's universality. The study systematically investigates the effects of HGB addition amount on the primer's thermal stability, resistance to chemical media, physical and mechanical properties, and hydrophobicity, focusing on evaluating its electrochemical anticorrosion performance and salt spray aging resistance. Meanwhile, an electrochemical workstation is used to deeply analyze the differences in anticorrosion mechanisms under different topcoat matching conditions. The overall aim is to devise an advanced waterborne anticorrosion coating system that combines long-term durability, environmental compatibility, and cost efficiency, thereby offering both theoretical insight and practical guidance toward industrial implementation of green anticorrosion technologies.

2. Materials and Methods

2.1. Experimental Materials

Raw lacquer was purchased from Maoba Lacquer in Enshi, Hubei, China; zirconium phosphate was purchased from Chengdu Huaxia Chemical Reagent Co., Ltd. in Chengdu, Sichuan, China; zinc powder was purchased from Jiangsu Jiaxin New Materials Co., Ltd. in Yancheng, Jiangsu, China; cetyltrimethylammonium bromide (CTAB), HGB, absolute ethanol, xylene, and ammonia water were purchased from Sinopharm Chemical Reagent Co., Ltd. in Shanghai, China; sodium alginate, tetrabutyl titanate, and dodecyltriethoxysilane (DTES) were purchased from Shanghai Aladdin Biochemical Technology Co., Ltd. in Shanghai, China; waterborne epoxy resin, waterborne polyester, and waterborne polyurethane were purchased from Jining Huakai Paint Co., Ltd. in Jining, Shandong, China.

2.2. Preparation of Materials

2.2.1. Preparation of AUZ/WEP Waterborne Composite Topcoat

6 g of ZrP and 19.3 g of CTAB were dispersed in 300 mL of distilled water and ultrasonicated until uniformly mixed, then reacted at room temperature for 2 h. After centrifugal washing, the product is labeled as CZrP. Sequentially, 3 g of CZrP, 4 g of tetrabutyl titanate, and 6 g of xylene were added to a 250 mL three-neck round-bottom flask and stirred vigorously at room temperature for 1 h; then, a mixture of xylene and urushiol was added dropwise, and the temperature was gradually raised to 80 °C for 1 h, 120 °C for 2 h, and 138 °C for 1 h. The resulting product is denoted as UTPCZrP. UTPCZrP, amphiphilic sodium alginate (APSA), and deionized water were added to a beaker in a ratio of 1 g:1 g:25 g, stirred uniformly, and then transferred to a ball mill for 4 h of ball milling to prepare the modifier AUZ. Finally, 5 wt% of AUZ was added to WEP and thoroughly mixed to obtain the AUZ/WEP composite coating. This concentration of 5 wt% AUZ was selected for the topcoat after preliminary tests confirmed it as the optimal loading to maximize the dispersion stability and barrier contribution of UTP and ZrP nanosheets without inducing aggregation, ensuring enhanced labyrinth effect and corrosion inhibition.

2.2.2. Preparation of HGB-Modified Waterborne Zinc-Rich Primer

0.6 g of HGB was slowly added to 10 g of WEP under magnetic stirring, stirred at 1000 r/min for 5 min until uniformly mixed, then 9.4 g of zinc powder was added, and the speed was increased to 1500 r/min for another 5 min of mixing. After ultrasonic defoaming, a 3% HGB-modified waterborne epoxy zinc-rich primer was obtained. Keeping WEP at 50 wt% of the total system mass, primers with zinc powder contents of 1.0 wt%, 2.0 wt%, and 3.0 wt% were prepared using the same method, as well as 2.0 wt% WPU and 2.0 wt% WPE modified zinc-rich primers. The 2 wt% HGB may be optimal based on preliminary theoretical and experimental assessments, which balanced the enhanced barrier

properties from HGB's labyrinth effect and defect-filling capability with the avoidance of agglomeration at higher concentrations.

2.2.3. Preparation of HGB-Modified Waterborne Zinc-Rich Primer Coatings and Matching Coatings

The prepared primers were uniformly applied onto polished tin-plated steel sheets (also known as tinplate) and glass slides. The surfaces were then dried at room temperature for 1 h, followed by drying in a blast drying oven at 80 °C for 2 h, resulting in the waterborne epoxy zinc-rich primer coatings. Some samples were further coated with a topcoat of WEP modified with 5.0 wt% AUZ on the primer surface. After drying using the same method, the matching coatings were obtained. The experimental groups were matching coatings with primer and topcoat, with addition amounts of 1.0 wt%, 2.0 wt%, and 3.0 wt%, labeled as: AUZ/Zn@HGB-1/WEP, AUZ/Zn@HGB-2/WEP, AUZ/Zn@HGB-3/WEP. The control groups were WEP, unmodified waterborne epoxy zinc-rich primer, and HGB-modified waterborne epoxy zinc-rich primer without topcoat, labeled as: WEP, Zn/WEP, Zn@HGB-1/WEP, Zn@HGB-2/WEP, Zn@HGB-3/WEP. The same method was used to prepare WPU and WPE matching coatings. The experimental groups were matching coatings with primer and topcoat, with an addition amount of 2.0 wt%, labeled as: AUZ/Zn@HGB-2/WPU, AUZ/Zn@HGB-2/WPE. The control groups were WPU, WPE, 2.0 wt% HGB-modified WPU zinc-rich primer, and 2.0 wt% HGB-modified WPE zinc-rich primer, labeled as: WPU, WPE, Zn@HGB-2/WPU, Zn@HGB-2/WPE.

2.3. Performance Test

2.3.1. Anticorrosion Performance Test

Tin-plated steel sheets (size 50 mm × 15 mm × 0.2 mm) sanded with 800-grit sandpaper were uniformly covered with a 110 ± 2 μm composite coating. Tin-plated steel sheet was selected as the substrate due to its uniform surface finish and consistent tin layer, which provides a standardized, passive surface ideal for reproducible coating application and reliable electrochemical testing, minimizing substrate-related variability. After complete drying, the exposed parts of the tin-plated steel sheets were sealed with a 1:1 mixture of rosin and paraffin, resulting in an exposed test area of ~2.5 cm^2 (approximately 1/3 of the total substrate surface area). The electrochemical workstation (CHI 660E, Shanghai Chenhua Instrument Co., Ltd., Shanghai, China) methods mainly included potentiodynamic polarization curves (Tafel) and electrochemical impedance spectroscopy (EIS). The test electrode consisted of a standard three-electrode system: working electrode (tin-plated steel sheet with coating), counter electrode (15 mm × 15 mm platinum electrode), and reference electrode (Ag/AgCl). The samples were placed in a 3.5 wt% NaCl solution and immersed for 1 h until the open circuit potential (OCP) stabilized. Test conditions were as follows: potential range of OCP ± 0.25 V, scan rate of 0.01 V/s, frequency range of 100,000 to 0.01 Hz, amplitude of 0.01 V. The NaCl solution was regularly replaced during testing to avoid interference from other impurities. Typically, Tafel polarization curves and EIS spectra are used to analyze the coating's anticorrosion performance. Polarization Tafel curves judge the coating's ability to protect the substrate by comparing corrosion currents. Generally, a smaller corrosion current indicates stronger corrosion resistance. As immersion days increase, EIS spectra can determine whether corrosion occurs through the capacitive arc, further evaluating the coating's anticorrosion performance.

2.3.2. Resistance to Liquid Media Test

According to GB/T 9274-1988 [17], the immersion method was used. Test solutions included 10 wt% H_2SO_4, 10 wt% NaOH, and 5 wt% NaCl. The experimental coatings

on tin-plated steel sheets were observed daily for discoloration, blistering, cracking, and peeling to evaluate their performance.

2.3.3. Physical and Mechanical Properties Test

a. Coating thickness: Referenced GB/T 13452.2-2008 (equivalent to ISO 2808:2019) [18], measured using HCC–24 magnetic resistance thickness gauge from Shanghai Huayang Testing Instrument Co., Ltd., Shanghai, China.
b. Gloss: Referenced GB/T 9754-2007 (equivalent to ISO 2813:2014) [19], measured 60° gloss using FR-60° gloss meter from Shanghai Farui Instrument Technology Co., Ltd., Shanghai, China.
c. Roughness: Referenced GB/T 1031-1995 (equivalent to ISO 4287:1997) [20], measured using TR200 handheld roughness tester from Time Group Inc., Beijing, China.
d. Pencil hardness: Referenced GB/T 6739-2006 (equivalent to ASTM D3363-23) [21], measured using pencil hardness tester from Shanghai Farui Instrument Technology Co., Ltd., Shanghai, China, range 6B–6H.
e. Flexibility: Referenced GB/T 6742-2007 (equivalent to ISO 1519:2012) [22], measured using QTX coating flexibility tester from Tianjin Yonglida Laboratory Equipment Co., Ltd., Tianjin, China.
f. Adhesion: Referenced GB/T 9286-2021 (equivalent to ISO 2409:2013) [23], measured using FR–3302 cross-cut adhesion tester from Shanghai Farui Instrument Technology Co., Ltd., Shanghai, China.g. Impact resistance: Referenced GB/T 1732-1993 (equivalent to ASTM D2794-23) [24], measured using QCJ-50/100 coating impact tester from Tianjin Shiboweiye Chemical Glass Instrument Co., Ltd., Tianjin, China.

2.3.4. Salt Spray Test

The corrosion resistance of the composite coatings was further characterized by salt spray testing. According to Chinese National Standard GB/T 1771–2007 [25], salt spray tests were conducted using a LYW–0.25 salt spray corrosion test chamber with a 5.0 wt% NaCl solution.

2.4. Characterization

The surface morphologies of HGB, zinc powder, and the coatings were observed using a Hitachi Regulus 8100 scanning electron microscope (SEM, Tokyo, Japan). Samples were sputter-coated with gold and imaged at an acceleration voltage of 5 kV. Elemental distribution analysis (EDS-Mapping) was performed at 10 kV. Fourier transform infrared (FTIR) spectra were recorded on a Thermo Fisher Nicolet iS 50 spectrometer (Waltham, MA, USA) using the ATR mode, with a wavenumber range of 400–4000 cm^{-1}, 32 scans, and a resolution of 4 cm^{-1}. Thermogravimetric analysis (TGA) was conducted on a NETZSCH STA 449 F3 thermal analyzer (Selb, Germany) under an air atmosphere, heating from 30 °C to 800 °C at a rate of 20 °C/min. Water contact angles (CA) were measured using a Krüss DSA30 instrument (Hamburg, Germany) via the sessile drop method, with deionized water as the medium; the reported value is the average of three measurements.

3. Results and Discussion

3.1. Material Characterization and Basic Coating Properties

Figure 1 presents scanning electron microscopy (SEM) images of hollow glass microspheres (HGB) and zinc powder at different magnifications. The HGB particles (Figure 1(A1–A3)) exhibit a relatively narrow particle size distribution, typically in the range of 5–20 μm, and display a near-Gaussian distribution profile. Their microstructure is characterized by highly regular, perfect spherical geometries with excellent sphericity

and structural integrity. The external surface of the HGB wall is generally smooth, devoid of significant large-area wrinkles or irregular undulations, although localized regions show subtle nanoscale roughness with sporadic adherence of fine particulate matter. In contrast, the zinc powder (Figure 1(B1–B3)) demonstrates a considerably broader particle size distribution, spanning approximately 10 to 100 μm, with a larger average particle size compared to HGB. Similarly, the zinc particles maintain a monodisperse, regularly spherical morphology under stacked conditions, but their surfaces appear noticeably smoother, with negligible wrinkling and only sporadic fine particle attachment. Collectively, HGB and zinc powder share fundamental similarities in their microstructural attributes, both belonging to the category of high-sphericity, continuously distributed particulate fillers. This structural commonality suggests potential interchangeability in certain composite formulations. The distinct advantages of HGB, namely its finer particle diameter and moderately rougher surface topology compared to zinc powder, are expected to promote stronger interfacial adhesion with matrix materials. This characteristic is likely to enhance dispersion stability within composite coatings and consequently improve overall application performance.

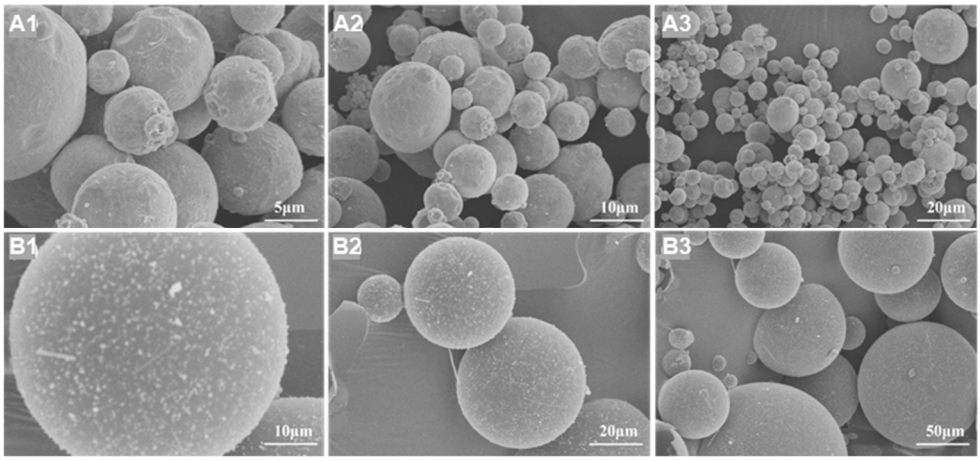


Figure 1. SEM images of (**A1**–**A3**) HGB and (**B1**–**B3**) zinc powder.

Figure 2 presents the Fourier-transform infrared (FT-IR) spectra of the waterborne composite coatings, with the baseline WEP spectrum (black line) exhibiting characteristic vibrational signatures of its molecular structure. The spectrum is dominated by the hydrophilic hydroxyl group stretching vibration at 3340 cm^{-1}, along with fingerprints of the epoxy resin backbone: symmetric and asymmetric C-H stretches of aliphatic groups at 2926 and 2856 cm^{-1}; aromatic -C=C- bending vibrations at 1728, 1528, and 1451 cm^{-1}; bending vibrations of the isopropylidene group -$C(CH_3)_2$- at 1317 cm^{-1} coupled with the asymmetric stretching of the C-O-C ether linkage at 1226 cm^{-1}. The distinct absorption bands in the 1200–1000 cm^{-1} region are assigned to C-O-C stretching vibrations of the epoxy rings, while the bending vibrations of the epoxy groups themselves appear between 950–800 cm^{-1}. Deformation vibrations of the epoxy rings are observed in the 870–750 cm^{-1} range [26]. Compared to the baseline, the matching coating system (e.g., green trace) exhibits a marked increase in the intensity of the hydroxyl band at 3340 cm^{-1}, which is attributed to the increased mass fraction of WEP in the topcoat formulation, which introduces a greater number of hydrophilic hydroxyl groups into the system. This interpretation is further supported by the enhanced intensity of characteristic epoxy signals at 1382, 1136, and 1035 cm^{-1}, consistent with the elevated WEP content in the final coating structure.

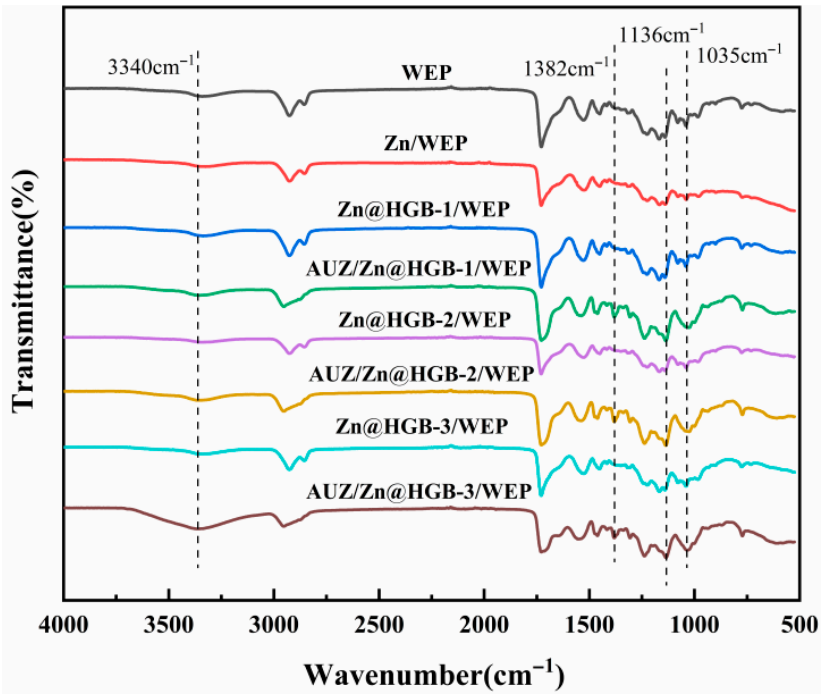


Figure 2. FT-IR spectra of water-based composite coatings.

Figure 3 compares the surface morphology for coatings with varying HGB content. The pristine WEP coating (Figure 3A) exhibits a porous and textured surface, with voids and irregular grooves formed during curing as water evaporates. Image analysis of SEM reveals that the porosity ratio of pristine WEP coating is approximately 12.3%, which compromises the coating compactness, potentially diminishing its corrosion resistance. The morphological differences observed are reproducible across multiple samples and are systematically linked to HGB content, not coincidental variations. Incorporation of zinc powder along with 1 wt% HGB (Figure 3B) results in a noticeable improvement in surface quality, where partial pore filling and reduced crack formation are observed. Correspondingly, the porosity ratio of the coating decreases to 6.7%, indicating enhanced compactness compared to pristine WEP. However, residual voids indicate insufficient defect remediation, suggesting that the combined addition of zinc and HGB at this concentration does not fully address the morphological imperfections. In contrast, the coating modified with 2 wt% HGB (Figure 3C) demonstrates a remarkably smooth and dense morphology, where the fine HGB particles effectively fill microcracks and eliminate most visible pores—yielding the best morphological integrity among the studied formulations, with its porosity ratio as low as 1.2% further confirming excellent compactness [27]. This trend is quantitatively supported by surface roughness data (Table 1), where the 2 wt% HGB formulation shows the lowest Ra value (0.624 μm), confirming its optimal compactness. Further increasing the HGB content to 3 wt% (Figure 3D) leads to agglomeration of excess modifier on the surface, reintroducing roughness and likely impairing anticorrosion performance. The porosity ratio of the coating rebounds to 8.9% due to the formation of voids caused by HGB agglomeration. The results underscore the efficacy of HGB as functional filler in mitigating the morphological defects of WEP. Owing to its sub-micron particle size, HGB provides superior pore-filling capability and enhances coating uniformity. The formulation with 2 wt% HGB achieves the highest degree of compactness, which is anticipated to correlate with enhanced barrier properties and superior long-term anticorrosion performance.

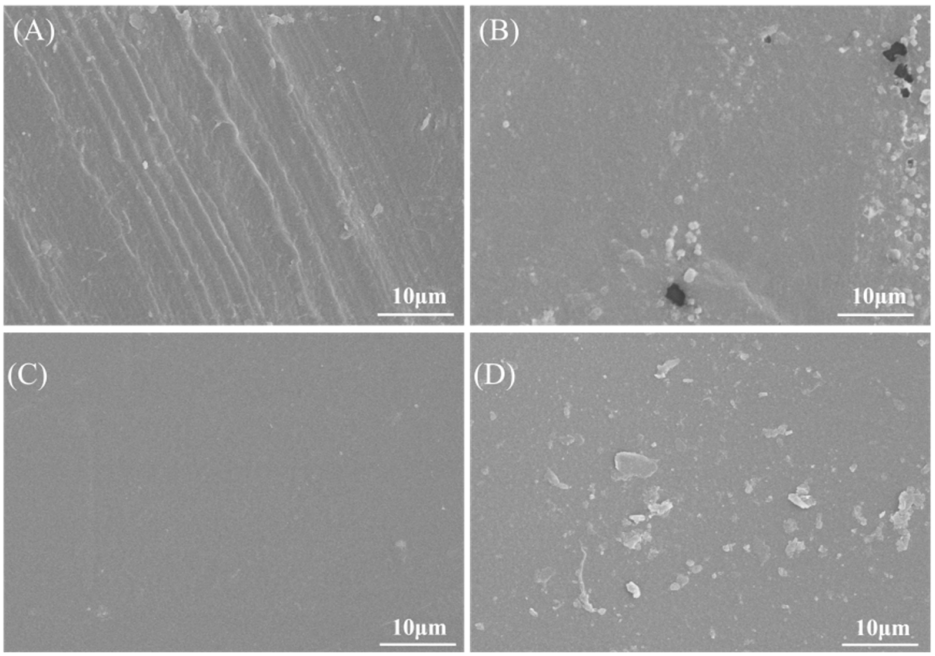


Figure 3. SEM images of (**A**) WEP, (**B**) Zn@HGB-1/WEP, (**C**) Zn@HGB-2/WEP, and (**D**) Zn@HGB-3/WEP.

Table 1. Physical and mechanical property of waterborne epoxy composite coatings.

Coating	60° Gloss (%)	Roughness (μm)	Pencil Hardness	Flexibility (mm)	Adhesion (Grade)	Impact Resistance (cm)
WEP	156.2	0.136	6H	0.5	0	95
Zn/WEP	5.8	0.815	6H	0.5	0	95
Zn@HGB-1/WEP	6.9	1.195	6H	1	0	95
Zn@HGB-2/WEP	14.9	0.624	6H	1	0	95
Zn@HGB-3/WEP	27.4	1.778	6H	1.5	0	95
AUZ/Zn@HGB-1/WEP	71.6	0.239	6H	1.5	0	95
AUZ/Zn@HGB-2/WEP	66.4	0.191	6H	1	0	95
AUZ/Zn@HGB-3/WEP	51.2	0.311	6H	4	0	95

Figure 4 presents a systematic elemental distribution analysis of the AUZ/Zn@HGB-2/WEP composite coating obtained through EDS-Mapping technology. The spatially resolved elemental maps (Figure 4A) reveal distinct distribution patterns of key constituents within the coating architecture. Carbon and oxygen elements (Figure 4B), constituting the WEP matrix, demonstrate homogeneous distribution throughout the coating cross-section, confirming the formation of a continuous polymer phase that provides fundamental physical support and barrier properties. Zinc element (Figure 4C) is localized in discrete regions corresponding to zinc powder particles within the primer layer, which provide cathodic protection. In contrast, silicon and boron (Figure 4D,E), characteristic components of HGB, display a complementary spatial relationship with zinc distribution, regions enriched with Si and B show corresponding depletion of Zn, providing direct evidence for the partial replacement of zinc powder by HGB microspheres. Titanium element (Figure 4F), indicative of the AUZ modifier, is evenly distributed, mainly in the near-surface region, suggesting its successful integration into the WEP matrix. This meticulously designed dual-layer coating architecture not only preserves the core sacrificial anode protection mechanism through zinc-rich regions but also optimizes the surface characteristics via HGB incorporation. The observed microstructural features demonstrate effective synergistic optimization among AUZ modifier, zinc powder, HGB carrier, and WEP matrix, establishing a structural foundation for enhanced comprehensive performance of the composite coating system.

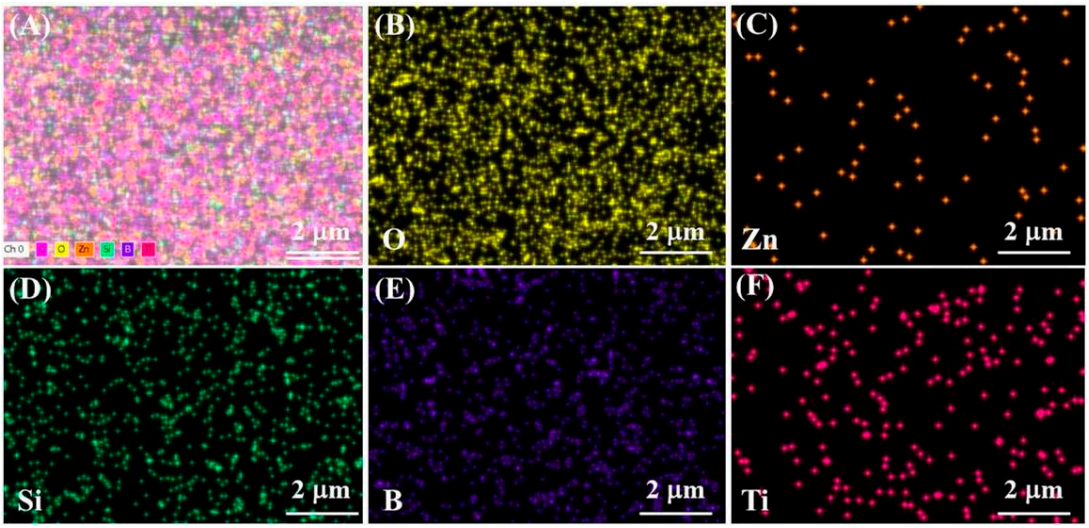


Figure 4. EDS-mapping diagram of AUZ/Zn@HGB-2/WEP composite coating: (**A**) selected elements, (**B**) O, (**C**) Zn, (**D**) Si, (**E**) B, (**F**) Ti.

3.2. Physical-Mechanical and Thermal Performance of Coatings

Table 1 summarizes the physical and mechanical properties of the various coating formulations. The pristine WEP exhibits excellent initial gloss (156.2%) and low surface roughness (0.136 μm), reflecting its good optical quality. The incorporation of zinc powder, however, significantly reduces the gloss to 5.8% and increases the roughness to 0.815 μm, which is attributed to the strong hiding power conferred by the inherent dark color of zinc particles. The subsequent introduction of HGB leads to a gradual recovery in gloss, from 6.9% for Zn@HGB-1/WEP to 27.4% for Zn@HGB-3/WEP, consistent with the light-colored nature of HGB. Notably, the coating containing 2 wt% HGB displays the lowest roughness (0.624 μm), which aligns with the smooth and dense morphology described in Figure 3C where the porosity ratio was only 1.2%, confirming that the optimal HGB content effectively improves both surface smoothness and compactness. In contrast, the Zn@HGB-3/WEP coating shows a relatively higher roughness value, which is consistent with the surface agglomeration phenomenon and increased porosity ratio (8.9%) observed in its SEM image. The introduction of urushiol–titanium polymer (AUZ) reduces the gloss further, to 71.6% for AUZ/Zn@HGB-1/WEP and 51.2% for AUZ/Zn@HGB-3/WEP, due to the inherent dark coloration of AUZ. In terms of flexibility, all modified coatings show some degree of deterioration (flexibility values ranging from 1 to 4 mm) compared to pure WEP (0.5 mm), suggesting that both HGB and AUZ have a negative influence on this property. It should be noted that the flexibility test was conducted according to GB/T 6742–2007, which has an operational deviation of up to 10% compared with ISO 1519:2012. Nevertheless, all modified coatings maintain the highest pencil hardness (6H), excellent adhesion (grade 0), and undiminished impact resistance (95 cm), confirming that the primer modification and topcoat matching strategy successfully preserves the key mechanical and protective properties of the coating system.

Thermogravimetric analysis was conducted to evaluate the effect of HGB incorporation on the thermal stability of the composite coatings. The thermal degradation process of the WEP-based coatings proceeds through three distinct stages (Figure 5). The first stage (30–250 °C), involving a mass loss of about 10%, is attributed to the evaporation of residual water and solvent, along with decomposition of low-molecular-weight oligomers. In the second stage (250–350 °C), the rate of mass loss increases markedly, resulting from the degradation of hard segments in WEP, small-molecular additives, and oxygen-containing functional groups introduced by modifiers [28]. Notable differences in mass loss are ob-

served among the coatings in this temperature range, with the unmodified WEP exhibiting a substantial loss of about 50%, while the modified formulations demonstrate significantly suppressed degradation. The final stage, between 350 and 450 °C, is characterized by the complete decomposition of the hard segments followed by rapid degradation of the well-ordered soft segments, accompanied by the collapse of the polymer architecture. The decomposition process stabilizes beyond 500 °C. The residual mass percentages at the endpoint of the test for WEP, Zn@HGB-1/WEP, Zn@HGB-2/WEP, Zn@HGB-3/WEP, AUZ/Zn@HGB-1/WEP, AUZ/Zn@HGB-2/WEP, and AUZ/Zn@HGB-3/WEP are 2.7%, 32.9%, 55.4%, 32.3%, 71.4%, 76.2%, and 76.6%, respectively. These findings clearly demonstrate that partial replacement of zinc powder with HGB significantly improves the thermal stability of the coatings, which can be ascribed to the excellent thermal insulation properties of the hollow glass microspheres. The enhancement is most pronounced at HGB loadings $\geq$ 2 wt%, which effectively mitigates surface defects within the composite, as corroborated by prior morphological analyses. Furthermore, the application of the AUZ-modified topcoat leads to an additional improvement in thermal stability, consistent with the synergistic effects observed in earlier performance evaluations.

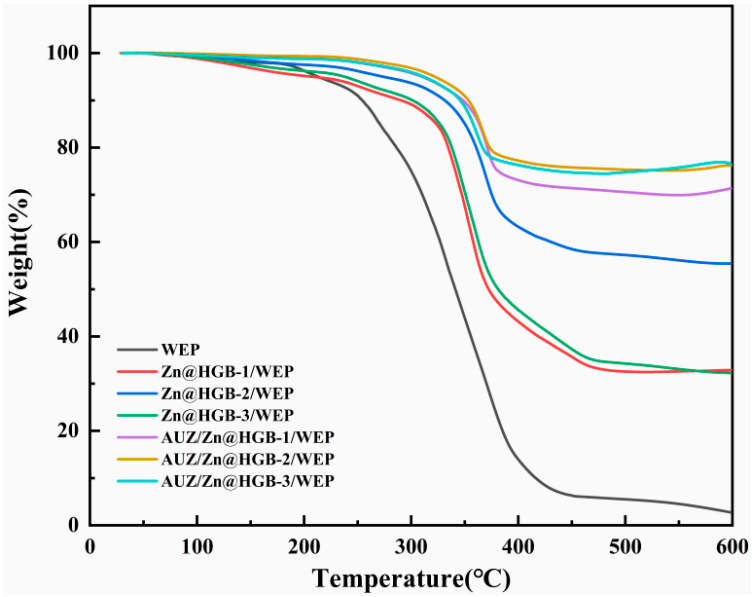


Figure 5. Thermogravimetric curve of waterborne epoxy composite coating.

3.3. Electrochemical Anticorrosion Performance

The surface wettability of the composite coatings was quantitatively assessed through water contact angle (CA) measurements (Figure 6). The pristine WEP exhibits a CA of 57.2°, indicating pronounced hydrophilic character. All modified coatings maintained CAs below 90°, remaining within the hydrophilic range, yet a marked increase in hydrophobicity was observed. This enhancement is attributed to the incorporation of hydrophobic constituents, specifically the urushiol–titanium polymer and zirconium phosphate (ZrP). Among the modified formulations, the coating with 2 wt% HGB addition demonstrated the most significant improvement, achieving a CA of 70.5°. This substantial increase suggests that HGB, functioning as an oleophilic-hydrophobic material, contributes effectively to hindering water penetration by altering the surface energy and microstructure of the composite. The enhanced hydrophobicity contributes to a more effective barrier against corrosive species, supporting the overall improvement in anticorrosion performance.

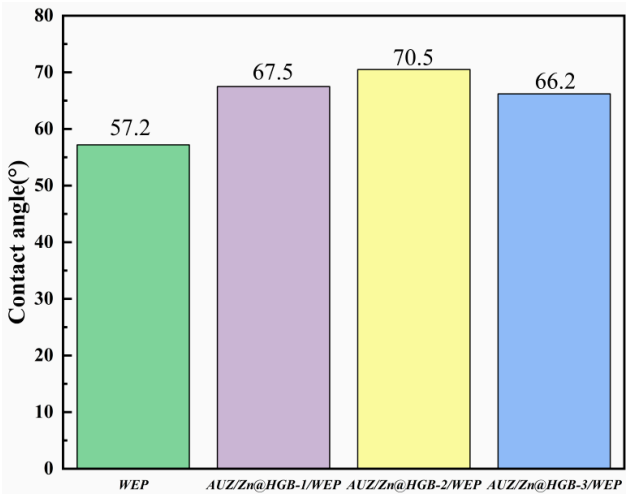


Figure 6. Water contact angles of different waterborne epoxy composite coatings.

The corrosion protection performance of the coating systems was evaluated through Tafel polarization measurements using a standard three-electrode configuration, where the coated sample served as the working electrode, a platinum plate as the counter electrode, and an Ag/AgCl electrode as the reference electrode. Each sample was immersed in a 3.5 wt% NaCl solution until the open-circuit potential (OCP) stabilized within the range of −0.4 V to −0.6 V. The polarization scan was then performed from OCP ± 0.25 V at a rate of 0.01 V/s to obtain the potential–current density curves. By analyzing these curves using the Tafel extrapolation method, key electrochemical parameters were derived, including corrosion potential (E_{cor}), corrosion current density (I_{cor}), polarization resistance (R_p), corrosion rate (CR), and protection efficiency (PE). The corresponding formulas are given as follows:

$$R_p = \frac{\gamma_\alpha \gamma_c}{2.303(\gamma_\alpha + \gamma_c) I_{cor}}$$

where γ_a and γ_c represent the anodic and cathodic Tafel slopes, respectively, and I_{cor} is the corrosion current density obtained from the intersection of the Tafel slopes.

$$CR(mm/year) = \frac{kM_m I_{cor}}{\rho_m}$$

where k is a constant, and M_m and ρ_m denote the atomic weight and density of the metal substrate, respectively.

$$PE = \frac{I_{cor,0} - I_{cor}}{I_{cor,0}} \times 100\%$$

where $I_{cor,0}$ refers to the corrosion current density of the bare metal substrate or the uncoated reference sample.

As illustrated in Figure 7, the Tafel curves of the different coatings exhibit clear differences in both shape and position, reflecting variations in their corrosion kinetics and protective properties. All Tafel curves were tested within a potential range of −1.0 V to −0.1 V, and the corrosion parameters were fitted within the standardized linear Tafel region of ±100 mV relative to the corrosion potential, with correlation coefficients (R^2) greater than 0.98 ensuring high fitting accuracy. Lower I_{cor}, higher R_p, and lower CR values generally indicate superior anticorrosion performance. The systematic inclusion of these parameters and their mathematical foundations allow for a rigorous comparison of the coating systems' efficacy in inhibiting corrosion under aggressive chloride conditions.

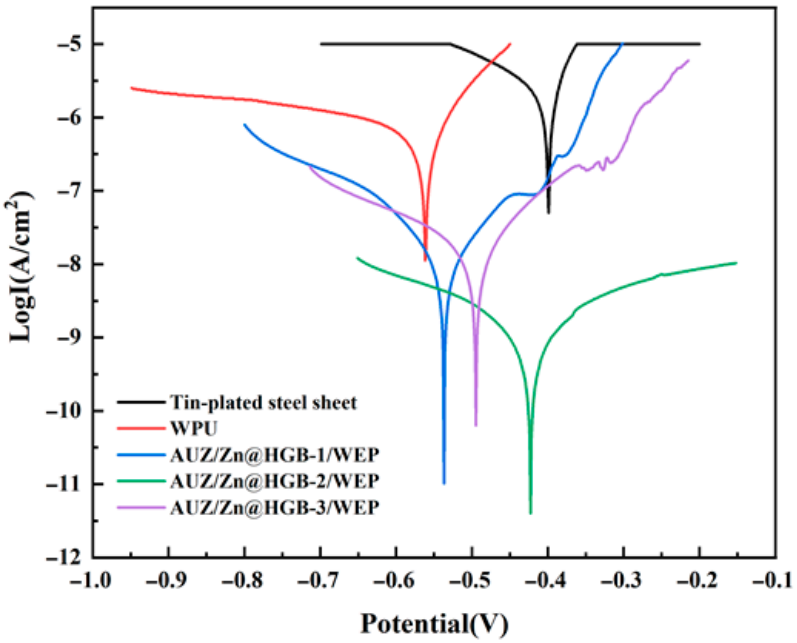


Figure 7. Tafel curves of different water-based epoxy composite coatings after immersion for 1 h (3.5 wt% NaCl).

Quantitative analysis of the derived parameters, summarized in Table 2, reveals a remarkable enhancement in corrosion resistance afforded by the coatings. The tin-plated steel sheet shows the highest I_{cor}, consistent with its high susceptibility to corrosion. The pure WEP coating reduces I_{cor} by three to four orders of magnitude, confirming a significant level of protection. This performance is substantially superior in the matching coating systems, a phenomenon attributed to the synergistic effect of the zinc-rich primer, which provides cathodic protection, and the AUZ-modified topcoat, where the UTP and two-dimensional ZrP nanosheets create an efficient physical barrier via a "labyrinth effect" that markedly hinders the penetration of corrosive species. Notably, the AUZ/Zn@HGB-2/WEP coating exhibits the most outstanding anti-corrosion properties, characterized by the lowest I_{cor} (1.54×10^{-9} A·cm^{-2}), the highest R_p (2.82×10^{7} Ω), and the slowest CR (5.71×10^{-6} mm/year). This superior performance demonstrates an effective synergistic protection mechanism, contrary to a merely porous system. The HGB-modified primer provides active cathodic protection at defects, as evidenced by the localized zinc distribution (Figure 4C) and active corrosion potential, while simultaneously enhancing the physical barrier through defect filling. The maintained cathodic protection capability, despite the HGB addition, is confirmed by the active corrosion potential, indicating the zinc-steel microcells remain functional and work synergistically with the physical barrier improved by HGB. This optimal performance aligns perfectly with the dense, defect-free morphology observed by SEM, which facilitates an effective physical barrier. The coating achieves a protection efficiency of 99.98% relative to the bare substrate, corresponding to a 97.38% improvement over pure WEP, confirming the success of the synergistic design strategy.

The corrosion protection performance of the coatings was evaluated by electrochemical impedance spectroscopy (EIS) in a 3.5 wt% NaCl aqueous solution. After 0.5–1 h of immersion, by which time the open-circuit potential (OCP) had stabilized, the EIS spectra of all coatings exhibited a single capacitive arc (Figure 8A,B), indicating effective physical barrier protection at the initial stage. Partial substitution of zinc powder with HGB in the primer resulted in a slight decrease in corrosion resistance, attributable to the superior cathodic protection provided by zinc powder, which forms a sacrificial anode

with the iron substrate. Among the HGB-modified primers, the formulation with 2 wt% HGB (Zn@HGB-2/WEP) exhibited the smallest impedance reduction, as the HGB particles helped fill microscopic defects and improve the structural integrity of the primer. The subsequent application of an AUZ-modified topcoat significantly enhanced the impedance of the coating system. Notably, the AUZ/Zn@HGB-2/WEP sample demonstrated the most pronounced enhancement in performance, exhibiting a remarkably high impedance value of 3.2×10^6 Ω. This value surpasses that of the primer-only system by two orders of magnitude, underscoring the profound efficacy of the composite design. With prolonged immersion, the protective performance evolution of the coatings became more distinct. After 2 days, the unmodified WEP coating showed obvious corrosion signs: a substantially reduced capacitive arc radius and phase angle changes in the Bode plot suggesting that corrosive media had penetrated to the substrate interface (Figure 8C,D). In contrast, primers modified with zinc powder and HGB continued to effectively hinder electrolyte penetration. However, Zn@HGB-1/WEP and Zn@HGB-3/WEP experienced significant impedance drops, whereas Zn@HGB-2/WEP maintained relatively stable performance, underscoring that an optimal HGB content is critical; deviations increase surface roughness and defect density, accelerating coating failure. After 10 days of immersion, all coatings experienced some impedance decrease, yet the matching coating systems showed no evident corrosion (Figure 8E,F). Notably, the AUZ/Zn@HGB-2/WEP coating still exhibited a higher impedance value than the initial value of the unmodified WEP after only 1 h of immersion, highlighting its potential for long-term protection. By day 25, the EIS spectrum of AUZ/Zn@HGB-3/WEP displayed two capacitive arcs, indicating that the electrolyte had reached the substrate (Figure 8G,H). In contrast, both AUZ/Zn@HGB-1/WEP and AUZ/Zn@HGB-2/WEP systems remained largely intact, demonstrating outstanding durability. These results confirm that although partial replacement of zinc powder with HGB yields a modest reduction in initial impedance, the synergistic interaction between HGB and zinc powder, which reaches optimal performance at 2 wt% HGB loading, significantly enhances the overall stability of the coating. The additional AUZ topcoat further significantly boosts impedance by leveraging the "labyrinth effect" of ZrP and UTP [29], which prolongs the diffusion path of corrosive species, enabling the dual-layer coating system to maintain excellent anti-corrosion performance even after 25 days of immersion [30]. The AUZ-modified topcoat, leveraging the "labyrinth effect" of UTP and ZrP, significantly prolongs the diffusion path of corrosive species, resulting in a dramatic impedance increase by two orders of magnitude. This synergy creates a composite barrier that effectively isolates the substrate, as confirmed by the sustained single capacitive arc in EIS spectra even after 25 days of immersion, demonstrating long-term stability that surpasses the unmodified coating.

Table 2. The fitted data of the Tafel curves of different water-based epoxy composite coatings after being immersed for 1 h (3.5 wt%NaCl).

Sample	E_{cor}/V	I_{cor}/A·cm^{-2}	R_p (Ω)	CR (mm/year)	PE/%		R^2
Tin-plated steel sheet	−0.522	3.24×10^{-4}	884.4				0.992
WEP	−0.523	5.87×10^{-8}	8.23×10^5	1.83×10^{-4}	99.41	0	0.988
AUZ/Zn@HGB-1/WEP	−0.537	2.08×10^{-8}	1.71×10^6	7.72×10^{-5}	99.79	64.57	0.990
AUZ/Zn@HGB-2/WEP	−0.423	1.54×10^{-9}	2.82×10^7	5.71×10^{-6}	99.98	97.38	0.995
AUZ/Zn@HGB-3/WEP	−0.495	2.10×10^{-8}	1.56×10^6	7.80×10^{-5}	99.08	64.22	0.987

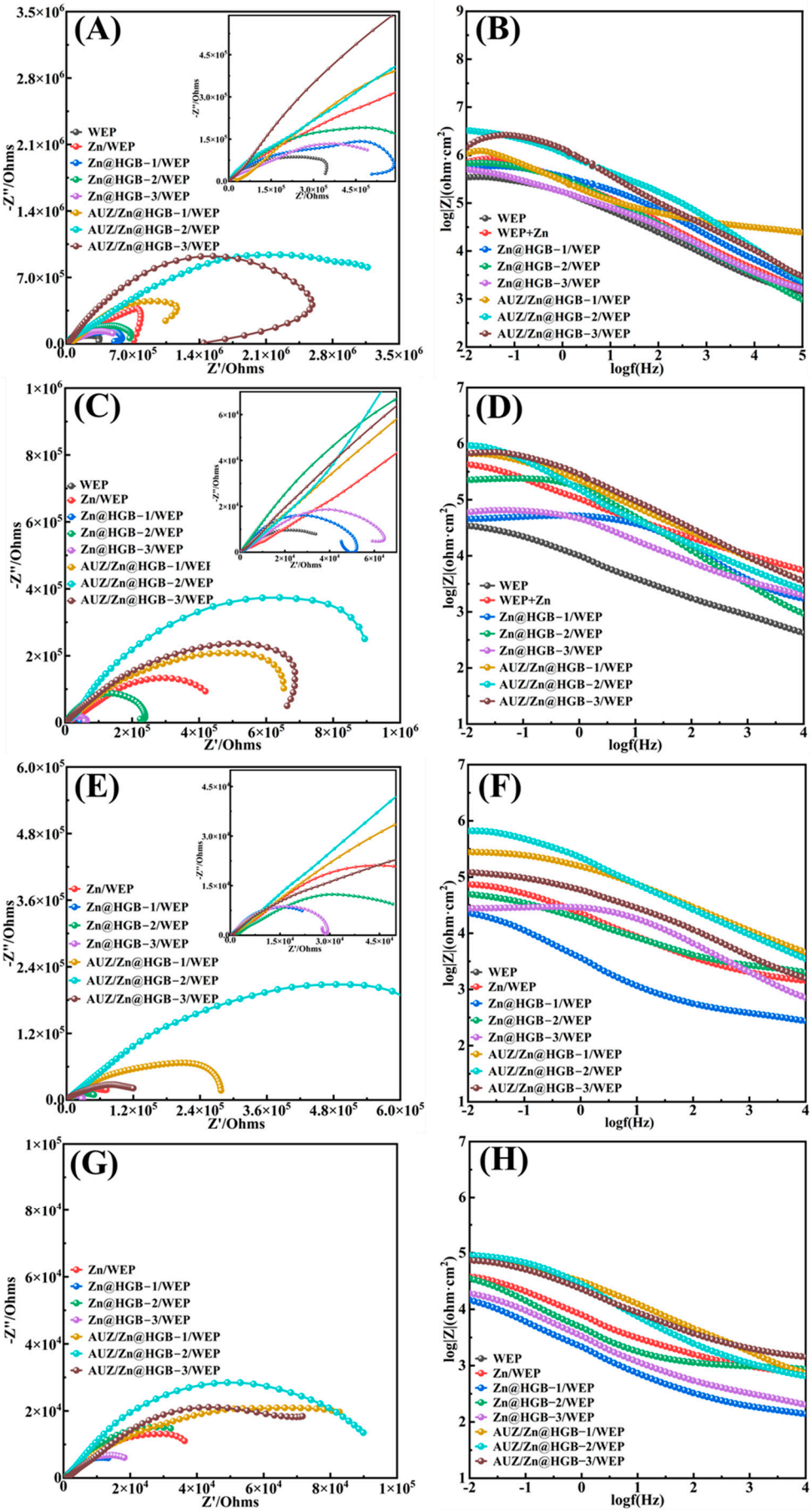


Figure 8. Nyquist plots and Bode plots of waterborne epoxy composite coatings at: 1 h (**A**,**B**), 2 d (**C**,**D**), 10 d (**E**,**F**), and 25 d (**G**,**H**).

3.4. Chemical and Environmental Durability Assessment

The resistance of the waterborne epoxy composite coatings to liquid media was evaluated by immersing specimens in acid, alkali, and salt solutions of different concentrations, following national standards. After 16 days of immersion, the changes in coating surface morphology were examined to assess corrosion resistance, as summarized in Table 3. In strongly alkaline environments (30 wt% and 10 wt% NaOH), all coated samples exhibited significant peeling, indicating poor alkali resistance and demonstrating that the primer–topcoat system used in this study did not substantially enhance performance under highly alkaline conditions. By contrast, in a 5 wt% NaCl solution, coatings without the topcoat showed noticeable detachment, revealing the limited salt resistance offered by zinc-rich primers alone. In contrast, the matching coating systems with an AUZ-modified topcoat remained intact throughout the 16-day immersion period. This improvement is attributed to the "labyrinth effect" resulting from the synergistic combination of ZrP and UTP within the AUZ modifier, which effectively impedes chloride ion penetration through enhanced physical barrier properties. Immersion tests in strong acid solutions revealed that coatings comprising only the zinc-rich primer exhibited limited resistance to acid corrosion in a 10 wt% H_2SO_4 solution. This is consistent with the high reactivity of zinc in acidic environments, as evidenced by the '-' notations in Table 3 for primer-only systems, which indicate observable changes such as discoloration or bubbling. In comparison, the matching composite coating systems remained largely intact after more than 16 days of immersion. When the acid concentration was increased to 30 wt% H_2SO_4, the matching systems displayed only slight discoloration after 16 days, with no severe corrosion damage. These results clearly indicate that the synergistic interaction between the AUZ modifier and the modified zinc-rich primer significantly enhances the acid resistance of the coating system. This improvement is primarily due to the inherent chemical stability of UTP in acidic environments, which imparts robust corrosion resistance. The synergistic combination of an AUZ-modified topcoat and an HGB-zinc-rich primer significantly enhances the coating system's resistance to salt-rich and highly acidic media. The composite coating can withstand approximately 16 days of immersion in such aggressive environments while maintaining structural integrity and showing no significant signs of corrosion, which is attributed to the "labyrinth effect" resulting from the synergistic combination of ZrP and UTP within the AUZ modifier [31–33].

Table 3. Results of liquid medium resistance performance of different waterborne epoxy composite coatings.

Coating	30%NaOH	10%NaOH	5%NaCl	10%H_2SO_4	30%H_2SO_4
WEP	–	–	–	–	–
Zn/WEP	–	–	–	–	–
Zn@HGB-1/WEP	–	–	–	–	–
Zn@HGB-2/WEP	–	–	–	–	–
Zn@HGB-3/WEP	–	–	–	–	–
AUZ/Zn@HGB-1/WEP	–	–	+	+	discoloured
AUZ/Zn@HGB-2/WEP	–	–	+	+	discoloured
AUZ/Zn@HGB-3/WEP	–	–	+	+	discoloured

Note: "+" indicates that the coating is intact without discoloration, bubbling, cracking or peeling. "−" indicates that the coating has changed color, bubbled, cracked or peeled off.

The corrosion resistance of the composite coatings was further evaluated through neutral salt spray testing using a 5 wt% NaCl solution, with continuous monitoring of corrosion progression along scribed areas and electrolyte penetration behavior. The initial states of each coating are shown in Figure 9(A1–F1). After 360 h of exposure, the zinc-rich primer coatings exhibited noticeable leaching of HGB particles, attributed to coating thinning caused by saline corrosion, which led to the exposure and release of micro-

spheres. Pronounced corrosion signs—including yellow oxidation products, substantial corrosion accumulation, coating delamination, and early-stage spread—were observed in both scribed and adjacent regions of the Zn@HGB-1/WEP (Figure 9(A2)) and Zn@HGB-3/WEP (Figure 9(C2)) coatings. In contrast, the Zn@HGB-2/WEP coating (Figure 9(B2)) displayed only minimal yellow corrosion products within the scribe, with markedly reduced coating detachment, indicating that the corrosive medium had reached the tin-plated steel substrate, but its progression was effectively suppressed [34]. When the test duration was extended to 720 h, the Zn@HGB-1/WEP (Figure 9(A3)) and Zn@HGB-3/WEP (Figure 9(C3)) coatings showed aggravated deterioration, characterized by abundant yellow–brown corrosion deposits and fine particulate accumulation at the metal-coating interface. Under prolonged exposure to high ion concentrations, corrosion intensified and spread laterally, reflecting inadequate protective performance. By comparison, the Zn@HGB-2/WEP coating (Figure 9(B3)) demonstrated significantly delayed corrosion progression, effective suppression of oxidation products, and no visible spreading tendency, confirming that the 2 wt% HGB addition provides an optimal physical barrier that effectively isolates the tin-plated steel substrate from corrosive species. These results underscore the critical role of HGB concentration, as deviations from the optimal 2 wt% loading clearly compromised coating performance.

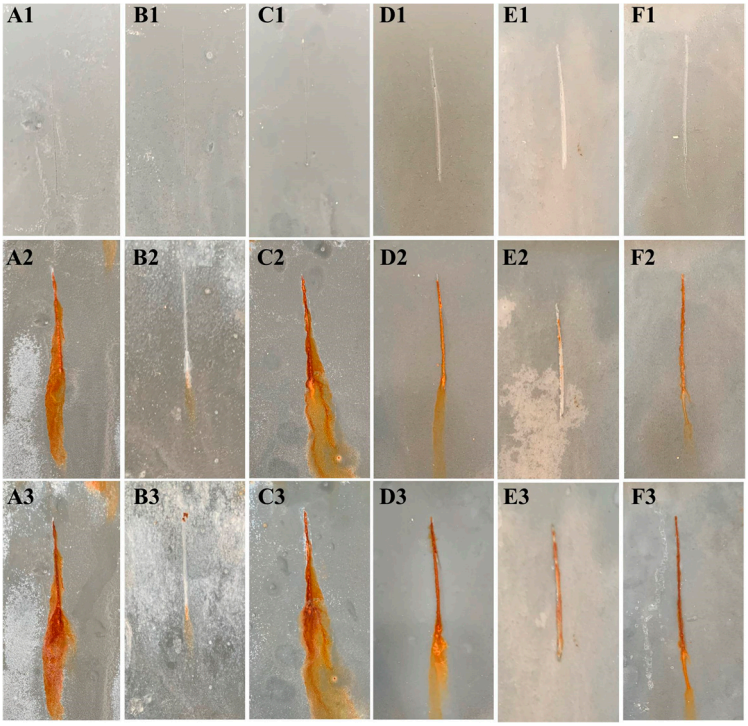


Figure 9. Optical photographs of the zinc-rich primer coating and the modified coating after neutral salt spray tests at different times: (**A**) Zn@HGB-1/WEP; (**B**) Zn@HGB-2/WEP; (**C**) Zn@HGB-3/WEP; (**D**) AUZ/Zn@HGB-1/WEP; (**E**) AUZ/Zn@HGB-2/WEP; (**F**) AUZ/Zn@HGB-3/WEP, where (**1**) 0 h, (**2**) 360 h, (**3**) 720 h.

The matching coating systems with an AUZ-modified topcoat exhibited further enhanced durability under the same salt spray conditions. After 360 h, the AUZ/Zn@HGB-1/WEP (Figure 9(D2)) and AUZ/Zn@HGB-3/WEP (Figure 9(F2)) coatings displayed yellow corrosion products within the scribe, deposited at the substrate interface. Although these products could potentially initiate corrosion spread under ionic activity, the extent of damage and lateral propagation were substantially lower than in the primer-only systems, with no significant sideways diffusion observed. This improvement is ascribed to the capability of UTP and ZrP

fillers to trap chloride ions and establish a labyrinth effect through their layered structure, thereby prolonging the diffusion path of corrosive media [35]. The AUZ/Zn@HGB-2/WEP sample (Figure 9(E2)) exhibited the best salt spray resistance, showing only minimal corrosion product formation and no diffusion along the coating-substrate interface. After 720 h, the AUZ/Zn@HGB-1/WEP and AUZ/Zn@HGB-3/WEP samples (Figure 9(D3,F3)) exhibited increased corrosion deposits and mild delamination, indicating accelerated interfacial deterioration due to ion accumulation and autocatalytic corrosion. Still, their performance remained superior to that of the uncoated primers. The AUZ/Zn@HGB-2/WEP coating (Figure 9(E3)) maintained excellent integrity with negligible corrosion spread and no delamination, demonstrating high surface smoothness and stability. This superior performance stems from the optimal HGB concentration and its synergy with the AUZ modifier, which together enhance the anticorrosion mechanism. In conclusion, the 2 wt% HGB-modified primer significantly improves the salt spray resistance of WEP, and the application of a 5 wt% AUZ topcoat further optimizes the protective performance, validating the designed dual-layer coating system as an effective strategy for long-term corrosion prevention.

3.5. Universality of the Coating Strategy in Other Resin Systems

Building upon the confirmed efficacy of the proposed methodology in significantly enhancing the anti-corrosion performance of WEP systems, we further extended its application to assess universality across aqueous WPU and WPE systems [36]. As illustrated by the Tafel polarization curves in Figure 10 and the corresponding fitting data in Table 4, both unmodified WPU and WPE coatings reduced the I_{cor} by one to two orders of magnitude relative to the bare tin-plated steel substrate. Given that a lower I_{cor} generally corresponds to improved corrosion resistance, this indicates that the base polymers themselves afford a basic degree of protection. More significantly, after modification with the AUZ/Zn@HGB composite system, the I_{cor} further decreased by an additional one to two orders of magnitude. Notably, the AUZ/Zn@HGB-2/WPE system exhibited the most pronounced improvement, with I_{cor} suppressed by two full orders of magnitude. These results strongly demonstrate that the integrated coating system—composed of an HGB-modified zinc-rich primer and an AUZ-modified topcoat—markedly enhances corrosion protection. The underlying mechanism can be attributed to the synergistic combination of a dense barrier effect, imparted by zirconium phosphate (ZrP) and urushiol–titanium polymer (UTP) within the AUZ component, together with mitigated internal stress and delayed permeation of corrosive species facilitated by HGB and zinc powder [37]. These findings collectively verify the broad applicability of the proposed modification strategy beyond WEP to other aqueous coating systems.

Complementing the I_{cor} results, the R_p and CR values followed consistent trends. After synergistic modification, the composite coatings exhibited markedly increased R_p alongside significantly reduced CR, corroborating the enhancements inferred from I_{cor}. In terms of PE, all modified coatings exhibited values exceeding 90%, underscoring a substantial improvement over their unmodified counterparts. Notably, the AUZ/Zn@HGB-2/WPE demonstrated exceptional performance, achieving PE values over 99% relative to both the bare substrate and the pristine WPE coating, indicating nearly complete corrosion suppression and highlighting the robustness of the optimized composite design. The uniform enhancement across these key electrochemical parameters reaffirms the universality and effectiveness of the modification approach when applied to WPU and WPE systems, and underscores the essential role of the synergy between HGB and AUZ in enhancing the durability of waterborne protective coatings.

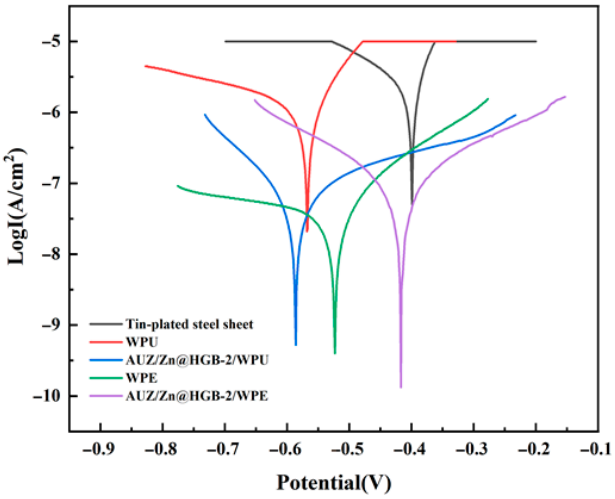


Figure 10. Tafel curves of two water-based composite coatings after immersion for 1 h (3.5 wt%NaCl).

Table 4. Tafel curve fitting Data of two water-based composite coatings after immersion for 1 h (3.5 wt%NaCl).

Sample	E_{cor}/V	I_{cor}/A·cm^{-2}	R_p (Ω)	CR (mm/year)	PE/%		R^2
Tin-plated steel sheet	−0.522	3.24×10^{-4}	884.4				0.992
WPU	−0.562	8.45×10^{-7}	4.09×10^{4}	2.63×10^{-3}	91.55	0	0.985
AUZ/Zn@HGB-2/WPU	−0.586	7.33×10^{-8}	4.85×10^{5}	2.72×10^{-4}	99.27	91.33	0.991
WPE	−0.568	2.36×10^{-6}	2.29×10^{4}	7.33×10^{-3}	76.40	0	0.983
AUZ/Zn@HGB-2/WPE	−0.417	9.25×10^{-8}	4.09×10^{5}	3.43×10^{-4}	99.07	99.61	0.993

Figure 11 presents the EIS analysis of unmodified and HGB-based primer-modified WPU and WPE coatings after different immersion times. During the initial 1 h immersion, the Nyquist plots of all coating systems exhibited a single capacitive arc, indicative of an effective protective function over the tin-plated steel substrate (Figure 11A,B) [38]. Notably, modification with the HGB based primer resulted in a substantial increase in impedance by one to two orders of magnitude. The matching modified WPU and WPE systems achieved impedance values of 3.57×10^6 Ω and 2.7×10^6 Ω, respectively, representing a two order of magnitude enhancement. The corresponding Bode plots corroborated the trends observed in the Nyquist plots. After 2 days, the unmodified WPU and WPE coatings displayed a second capacitive arc in their Nyquist plots, suggesting that the corrosive medium had penetrated to the coating metal interface and initiated corrosion, which is attributed to inherent porosity and defects that facilitate electrolyte penetration (Figure 11C,D) [39]. In contrast, the modified composite coatings, particularly the matching primer topcoat systems, maintained significantly higher impedance values, by one to two orders of magnitude, confirming that the synergistic interaction between the primer and topcoat effectively hindered the corrosion process [40]. Although the primer-only samples showed a relatively faster impedance decrease, they still outperformed the unmodified coatings. After 10 days of immersion, the modified composite coatings showed a slight reduction in the capacitive arc radius, yet the absence of a second capacitive arc in the Nyquist plots indicated that the coating metal interface remained largely intact without significant corrosive reaction, preserving the barrier function (Figure 11E,F). Even after 25 days of immersion, all four modified coating systems maintained a single capacitive arc, providing further evidence of their sustained and effective protection of the substrate (Figure 11G,H).

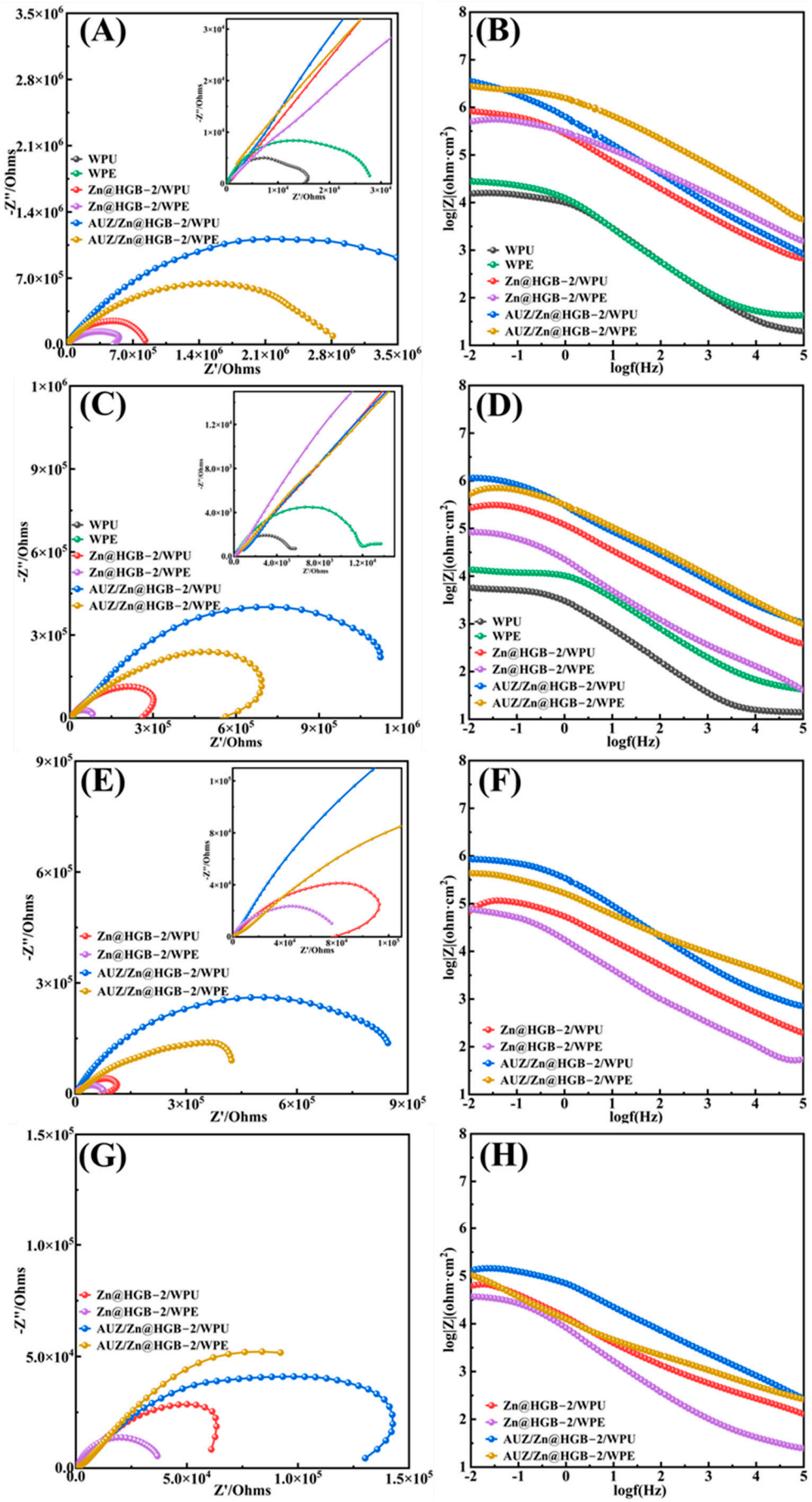


Figure 11. Nyquist plots and Bode plots of two water-based composite coatings at: 1 h (**A**,**B**), 2 d (**C**,**D**), 10 d (**E**,**F**), and 25 d (**G**,**H**).

The proposed anti-corrosion mechanism is illustrated in Figure 12. Initially, the unmodified waterborne epoxy coating exhibits inherent micro-defects such as pores and cracks, through which corrosive species (O_2, H_2O, Cl^-) penetrate directly toward the tin-plated steel substrate [41,42]. This is supported by the SEM observations of a porous WEP surface and the small capacitive arc in early EIS spectra, indicating limited barrier properties. The HGB-modified waterborne epoxy zinc-rich primer, formulated by replacing 20 wt% of zinc particles with HGB, retains residual zinc particles that provide initial cathodic protection; their subsequent corrosion products further seal micro-pores in the primer layer, reinforcing the barrier effect. Subsequently, the incorporation of UTPCZrP nanosheets into the topcoat induces a "maze effect", forcing corrosive media to follow a tortuous diffusion path rather than a straight-line penetration [43,44]. The notable increase in impedance and the characteristic FTIR peaks confirm the effective introduction of UTPCZrP, while salt spray tests demonstrate suppressed corrosion spread. Ultimately, the synergistic action of HGB and UTPCZrP leads to the formation of a dense, three-dimensional barrier: HGB particles fill defects in the primer layer, mitigating stress concentration, while UTPCZrP nanosheets stack tightly in the topcoat, collectively blocking the permeation of corrosive media.

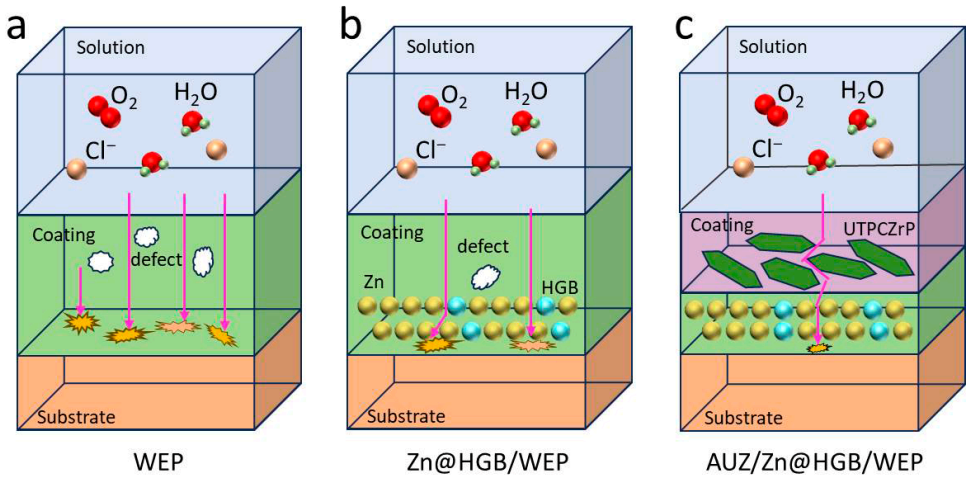


Figure 12. Synergistic anticorrosion mechanism of HGB and UTPCZrP.

4. Conclusions

The synergistic integration of a designed HGB-modified waterborne epoxy primer with a 5 wt% AUZ-modified epoxy topcoat, based on a rational design strategy aimed at cost reduction and performance enhancement, has yielded a composite coating system with markedly enhanced corrosion protection performance. This optimized system exhibits superior thermal stability, with a residual char yield as high as 76.6%, along with excellent chemical resistance, withstanding immersion in aggressive acid and salt solutions for 16 days without major degradation. While maintaining high-level physical and mechanical properties, the coating demonstrates a remarkable 1–2 order-of-magnitude improvement in anti-corrosion metrics. The optimal formulation, achieved with a 2 wt% HGB loading, after systematic evaluation of 1–3 wt% concentrations, which provided the optimal coating compactness and the highest electrochemical performance due to synergistic effects between HGB and AUZ, displays an impedance value of 3.2×10^6 Ω, an exceptionally low corrosion rate of 5.71×10^{-6} mm/year, and a protection efficiency of 99.98%, with stable performance sustained over 25 days of immersion. Salt spray testing further confirmed the significantly enhanced durability, wherein the AUZ/Zn@HGB-2/WEP coating showed no corrosive medium diffusion after 720 h. The broad applicability of this approach was demonstrated in WPU and WPE systems, where the corresponding composite coatings reached impedance

values of 3.57 × 10^6 Ω and 2.7 × 10^6 Ω, respectively, alongside a corrosion protection improvement exceeding 90% with long-term stability. These findings collectively affirm the efficacy and broad applicability of the HGB/AUZ synergistic strategy for developing high-performance, environmentally friendly anti-corrosion coatings.

Author Contributions: X.Z.: data curation, writing—original draft, methodology, investigation, writing—review and editing. R.M.: investigation. M.L.: data curation. J.C.: resources, investigation, formal analysis. F.L.: resources, methodology. D.W.: resources, data curation, validation. G.Z.: software. Y.X.: validation, supervision, funding acquisition. Q.L.: conceptualization, funding acquisition, project administration. All authors have read and agreed to the published version of the manuscript.

Funding: We acknowledge the generous financial support of the National Natural Science Foundation of China (Grant Nos. 32572000, 32501595, 52303355), Natural Science Foundation of Fujian Province (Grant Nos. 2023J011574, 2024J08279), the Science and Technology Project of the Fuzhou Institute of Oceanography (Grant No. 2025F20), the Collaborative Innovation Initiative by the Fuzhou Science and Technology Bureau with Municipal Universities and Research Institutes (Grant No. 2024–SG–010), Fuzhou–Xiamen–Quanzhou National Independent Innovation Demonstration Zone Collaborative Innovation Platform Project (Grant No. 2025–P–006), the "Open Competition Mechanism to Select the Best Candidates" Project of Minjiang University (Grant No. ZD202302).

Institutional Review Board Statement: Not applicable.

Informed Consent Statement: Not applicable.

Data Availability Statement: Data are contained within the article.

Conflicts of Interest: The authors declare that they have no competing interests.

Abbreviations

The following abbreviations are used in this manuscript:

HGB	Hollow glass microspheres
UTP	Urushiol titanium polymer
WPU	Waterborne polyurethane
WPE	Waterborne polyurethane and polyester
VOCs	Volatile organic compounds
WEP	Waterborne epoxy resin
CTAB	Cetyltrimethylammonium bromide
DTES	Dodecyltriethoxysilane
APSA	Amphiphilic sodium alginate
EIS	Electrochemical impedance spectroscopy
OCP	Open circuit potential
CA	Contact angles
AUZ	Introduction of urushiol–titanium polymer
ZrP	Zirconium phosphate
CR	Corrosion rate
E_{cor}	Corrosion potential
I_{cor}	corrosion current density
R_p	Polarization resistance
PE	Protection efficiency

References

1. Ren, A.; Kang, M.; Fu, X. Corrosion behaviour of Ni/WC-MoS_2 composite coatings prepared by jet electrodeposition with different MoS_2 doping concentrations. *Appl. Surf. Sci.* **2023**, *613*, 155905. [CrossRef]
2. Zehra, S.; Mobin, M.; Aslam, J. An overview of the corrosion chemistry. *Environ. Sustain. Corros. Inhib.* **2022**, *1*, 3–23.

3. Mei, D.; Li, Y.; Tian, Y.; Zhang, Q.; Liu, M.; Zhu, S.; Wang, L.; Guan, S. The effect of selected corrosion inhibitors on localized corrosion of magnesium alloy: The expanded understanding of "inhibition efficiency". *Corros. Sci.* **2024**, *226*, 111650. [CrossRef]
4. Cui, J.; Bao, Y.; Sun, Y.; Wang, H.; Li, J. Critical factors on corrosion protective waterborne coatings containing functionalized graphene oxide: A review. *Compos. Part A-Appl. Sci. Manuf.* **2023**, *174*, 107729. [CrossRef]
5. Guan, H.; Zhang, D.; Liu, Z.; Ding, Y.; Liu, Q. Toughening and corrosion resistance enhancement of waterborne epoxy films via polyurethane-based reactive epoxy emulsifier and capping agents. *J. Mater. Sci.* **2025**, *60*, 20110–20125. [CrossRef]
6. Ibarhiam, S.F.; Alzahrani, S.O.; Snari, R.M.; Aldawsari, A.M.; Alhasani, M.; Saad, F.; El-Metwaly, N.M. Novel multifunctional acrylic paint from sugarcane bagasse: Photoluminescence, photochromism, hydrophobicity and anticorrosion. *Mater. Today Commun.* **2022**, *33*, 104703. [CrossRef]
7. Sreehari, H.; Sethulekshmi, A.S.; Saritha, A. Bio epoxy coatings: An emergent green anticorrosive coating for the future. *Macromol. Mater. Eng.* **2022**, *307*, 2200004. [CrossRef]
8. He, L.; Hou, Y.; Yang, F. Study of the properties of Waterborne Epoxy Resin Emulsified asphalt and its modification mechanism. *J. Mater. Civ. Eng.* **2023**, *35*, 04023145. [CrossRef]
9. Wang, H.; Chen, Z.; Wang, L.; Zhao, Q.; Zeng, B.; Xu, Y.; Chen, G.; Luo, W.; Yuan, C.; Dai, L. α-Zirconium Phosphate Hybrid Intercalated by Carbon Dots with High Anticorrosion Efficiency for Waterborne Epoxy Resin Composite Coating. *ACS Appl. Mater. Interfaces* **2025**, *17*, 17368–17380. [CrossRef]
10. Qi, C.; Dam-Johansen, K.; Wu, H. Engineering of zinc-bismuth binary microspheres and evaluation of ZnBi-rich primer for corrosion protection of steel in marine environment. *J. Mater. Sci. Technol.* **2025**, *241*, 138–149. [CrossRef]
11. Lv, X.; Jin, X.; Zhang, Z.; Bai, Y.; Guo, T.; Zhang, L.; Zhang, H.; Zhu, J.; Shao, Y.; Zhang, H. Comparative study of carbonaceous and polymer conductive additives on anticorrosion performance of epoxy Zinc-rich primer. *Coatings* **2022**, *12*, 1473. [CrossRef]
12. Xu, B.; Li, T.; Sun, Q.; Lou, Z.; Chen, S.; Li, W. Hierarchically structured superhydropobic polydimethylsiloxane composite film for daytime radiative cooling. *J. Mater. Sci.* **2025**, *60*, 7909–7923. [CrossRef]
13. Gogoi, R.; Kumar, N.; Mireja, S.; Ravindranath, S.S.; Manik, G.; Sinha, S. Effect of hollow glass microspheres on the morphology, rheology and crystallinity of short bamboo fiber-reinforced hybrid polypropylene composite. *Jom* **2019**, *71*, 548–558. [CrossRef]
14. Ding, J.; Liu, Q.; Zhang, B.; Ye, F.; Gao, Y. Preparation and characterization of hollow glass microsphere ceramics and silica aerogel/hollow glass microsphere ceramics having low density and low thermal conductivity. *J. Alloys Compd.* **2020**, *831*, 154737. [CrossRef]
15. Dong, W.; Qian, D.; Xi, Y.; Peng, J.; Hong, W.; Luo, Y.; Bai, Y.; Zhu, S. Preparation and properties of waterborne polyurethane coatings containing polyurethane-coated hollow glass microspheres. *Prog. Org. Coat.* **2025**, *208*, 109490. [CrossRef]
16. Chen, F.; Cheng, S.; Zhang, G.; Chen, S.; Yang, R. Development of ultralightweight cement composites with low density and high-specific strength using hollow glass microspheres. *J. Mater. Civ. Eng.* **2021**, *33*, 04021124. [CrossRef]
17. *GB/T 9274-1988*; Paints and Varnishes—Determination of Resistance to Liquids. Standards Press of China: Beijing, China, 1988.
18. *GB/T 13452.2-2008*; Paints and Varnishes—Determination of Film Thickness. Standards Press of China: Beijing, China, 2008.
19. *GB/T 9754-2007*; Paints and Varnishes—Determination of Specular Gloss. Standards Press of China: Beijing, China, 2007.
20. *GB/T 1031-1995*; Geometrical Product Specifications (GPS)—Surface Roughness Parameters and Their Values. Standards Press of China: Beijing, China, 1995.
21. *GB/T 6739-2006*; Paints and Varnishes—Determination of Pencil Hardness of Films. Standards Press of China: Beijing, China, 2006.
22. *GB/T 6742-2007*; Paints and Varnishes—Bend Test (Cylindrical Mandrel). Standards Press of China: Beijing, China, 2007.
23. *GB/T 9286-2021*; Paints and Varnishes—Cross-Cut Test. Standards Press of China: Beijing, China, 2021.
24. *GB/T 1732-1993*; Paints and Varnishes—Determination of Impact Resistance of Films. Standards Press of China: Beijing, China, 1993.
25. *GB/T 1771-2007*; Paints and Varnishes—Determination of Resistance to Neutral Salt Spray. Standards Press of China: Beijing, China, 2007.
26. Nan, D.; Li, X.; Li, D.; Liu, Q.; Wang, B.; Gao, X.; Ma, T.; He, N.; Xu, Y.; Dong, J. Preparation and anticorrosive performance of waterborne epoxy resin composite coating with amino-modified graphene oxide. *Polymers* **2022**, *15*, 27. [CrossRef]
27. Pei, L.; Lin, D.; Yuan, S.; Lu, R.; Bai, Z.; Sun, Y.; Zhu, Y.; Jiang, Y.; Zhu, J.; Wang, H. A multifunctional and long-term waterborne anti-corrosion coating with excellent 'hexagonal warrior'properties. *Chem. Eng. J.* **2023**, *457*, 141158. [CrossRef]
28. Zhao, H.; Liang, X.; Gao, Y. Organic-inorganic hybrid epoxy resin coating with high thermal stability and hydrophobicity for corrosion protection prepared by (3-aminopropyl) triethoxysilane as a bridging agent. *Mater. Today Commun.* **2024**, *39*, 108950. [CrossRef]
29. Tang, S.; Wang, T.; Xu, P.; Ge, W.; Chen, J.; Guo, H.; Feng, Z.; Lei, B.; Zhang, P.; Meng, G. Maze Effect or Antimaze Effect: The Double Effect of Modified 2D Fillers $Ti_3C_2T_x$ on the Properties of Waterborne Polyurethane Coatings. *ACS Appl. Mater. Interfaces* **2025**, *17*, 21745–21759. [CrossRef]
30. Sun, J.; Xiao, X.; Meng, G.; Gu, L. Mussel-inspired hydrophobic modification of boron nitride nanosheets to enhance the dispersion and anticorrosive performance in polymeric coatings. *Prog. Org. Coat.* **2022**, *170*, 106986. [CrossRef]

31. Han, P.; Tu, X.; Chen, L.; Du, P. Fabrication and performance of PES/Al composite corrosion-resistant coating based on labyrinth effect structure. *Mater. Des.* **2025**, *256*, 114313. [CrossRef]
32. Huang, R.; Wang, Y.; Zhou, Y.; Lei, J.; Feng, Q.; Ye, T.; Liu, Z.; Tang, D. Strategies to improve the anti-corrosion of Al alloy substrate effectively by reinforced double interfacial adhesion and enhanced penetration resistance of labyrinth effect. *Prog. Org. Coat.* **2025**, *208*, 109447. [CrossRef]
33. Li, H.; Xue, C.; Gao, L.; Wang, X.; Wei, H.; Nan, H.; Wang, G.; Lin, H. "Labyrinthine structure" anticorrosive water-based composite coatings. *Prog. Org. Coat.* **2021**, *150*, 105974. [CrossRef]
34. Peng, J.; Xiao, J.; Yang, Y.; Dong, Y.; Zhang, J. Long-term experimental study and prediction of the mechanical performance on corroded prestressing steel strands subjected to marine salt spray environment. *Constr. Build. Mater.* **2024**, *425*, 136069. [CrossRef]
35. Wu, B.; Yan, D.; Lin, J.; Song, J. Wire electrochemical etching of superhydrophobic nickel surfaces with enhanced corrosion protection. *Materials* **2023**, *16*, 7472. [CrossRef]
36. Khalaf, M.M.; Abd El-Lateef, H.M.; Abou Taleb, M.F.; Gouda, M. Graphene nanosheet reinforcement of polyurethane nanocomposite for green and sustainable photoluminescence, superhydrophobic, and anticorrosive paint. *Luminescence* **2024**, *39*, e4753. [CrossRef]
37. Zhang, Y.; Zhou, Y.; Ban, L.; Tang, T.; Liu, Q.; Liu, X.; He, J. Cu–Ethanolamine Nanozymes Promote Urushiol Oxidation of Lacquer. *Coatings* **2024**, *14*, 332. [CrossRef]
38. Akbarinezhad, E.; Rezaei, F.; Neshati, J. Evaluation of a high resistance paint coating with EIS measurements: Effect of high AC perturbations. *Prog. Org. Coat.* **2008**, *61*, 45–52. [CrossRef]
39. Odhiambo, J.G.; Li, W.; Zhao, Y.; Li, C. Porosity and its significance in plasma-sprayed coatings. *Coatings* **2019**, *9*, 460. [CrossRef]
40. Lin, J.; Orgon, C.; Battocchi, D.; Bierwagen, G.P. (Mg rich primer-powder topcoat) coating system for the corrosion protection of Al alloys. *Prog. Org. Coat.* **2017**, *102*, 138–143. [CrossRef]
41. Tabish, M.; Zhao, J.; Kumar, A.; Yan, J.; Wang, J.; Shi, F.; Zhang, J.; Peng, L.; Mushtaq, M.A.; Yasin, G. Developing epoxy-based anti-corrosion functional nanocomposite coating with CaFe-Tolyl-triazole layered double hydroxide@ g-C_3N_4 as nanofillers on Q235 steel substrate against NaCl corrosive environment. *Chem. Eng. J.* **2022**, *450*, 137624. [CrossRef]
42. Su, Y.; Qiu, S.; Wei, J.; Zhu, X.; Zhao, H.; Xue, Q. Sulfonated polyaniline assisted hierarchical assembly of graphene-LDH nanohybrid for enhanced anticorrosion performance of waterborne epoxy coatings. *Chem. Eng. J.* **2021**, *426*, 131269. [CrossRef]
43. Shao, Z.; Ren, P.; Jia, T.; Lei, B.; Feng, Z.; Guo, H.; Chen, S.; Zhang, P.; Meng, G. High-pressure induced acceleration pathways for water diffusion in heavy duty anticorrosion coatings under deep ocean environment: (I) The samples subjected to high-pressure pre-processing. *Prog. Org. Coat.* **2022**, *170*, 106948. [CrossRef]
44. Cai, M.; Fan, X.; Yan, H.; Li, Y.; Song, S.; Li, W.; Li, H.; Lu, Z.; Zhu, M. In situ assemble $Ti_3C_2T_x$ MXene@MgAl-LDH heterostructure towards anticorrosion and antiwear application. *Chem. Eng. J.* **2021**, *419*, 130050. [CrossRef]

Disclaimer/Publisher's Note: The statements, opinions and data contained in all publications are solely those of the individual author(s) and contributor(s) and not of MDPI and/or the editor(s). MDPI and/or the editor(s) disclaim responsibility for any injury to people or property resulting from any ideas, methods, instructions or products referred to in the content.